Modelling of anomalies due to hydrophones in continuous-wave ultrasound fields

Tomi Huttunen, Jari P. Kaipio and Kullervo Hynynen

Abstract

Needle and spot-poled membrane hydrophones employing polyvinylidene fluoride (PVDF) sensors are widely used for characterization of biomedical ultrasound fields. It is known that in measurements of continuous-wave (CW) fields, standing waves may be generated between the transducer and the hydrophone, distorting the field and possibly alternating the signal of the hydrophone. This study utilizes a three dimensional full-wave method to computationally simulate the distortion in the CW field caused by needle and membrane hydrophones. The physical model used in simulations is based on the linear time-harmonic wave equation which therefore neglects the effects of nonlinear wave propagation.

The significance of the distortion is examined by comparing fields emitted by 0.5-5.0 MHz planar circular transducers in the absence and presence of the hydrophones. In addition, the effect of the field distortions on the signal of the hydrophones is studied with simulated measurements.

The simulations showed an observable standing wave pattern between the source and the needle hydrophone if the diameter of the needle was larger than a half of the wavelength. However, the standing waves had not clear effect on the signal of the hydrophone. The presence of membrane hydrophone in the CW field generated notable standing waves. Furthermore, the standing waves caused a periodic distortion to the signal of the membrane hydrophone.

I. INTRODUCTION

Hydrophones that utilize the piezo-electricity of polyvinylidene fluoride (PVDF) films are widely used for measuring ultrasound fields. Since the discovery of piezo-electricity of PVDF in the late 1960's, polymer hydrophones have become standards in the characterization of medical ultrasound fields [1]. PVDF has several attractive features over many piezo-materials including, for example, high sensitivity,

T. Huttunen is with the Department of Applied Physics, University of Kuopio, Finland and Brigham and Women's Hospital, Harvard Medical School

J.P. Kaipio is with the Department of Applied Physics, University of Kuopio, Finland

K. Hynynen is with the Brigham and Women's Hospital, Harvard Medical School

close acoustic impedance match with water and a relatively flat frequency response. In addition, availability of PVDF in thin (a few μm thick) sheets makes it an ideal material for hydrophones for detecting sound waves in megahertz frequencies. Various hydrophone models have been developed [1] of which, two commonly used types of hydrophones in biomedical applications are needle(probe) and spot-poled membrane hydrophones [2].

A needle hydrophone consists of a hollow metallic needle and a thin, usually 9-25 μm, PVDF film mounted onto the tip of the needle. The film contains electrodes and is backed with a material suitable for preventing reflection of waves from the inner end of the film. To obtain good spatial resolution, the diameter of the needle and the active area of the film are small, typically between 0.3-1.5 mm and 0.04-1.0 mm, respectively. Advantages and basic constructions of needle hydrophones are discussed further in [3].

A spot-poled membrane hydrophone consists of a PVDF film supported only at the edges by a mounting ring. The typical thickness of the film is 9-100 μm and diameter can be as large as 100 mm. The film may consist of single, or more recently, two sheets of the PVDF and very thin (e.g 25 nm) layers of a nonpiezo-electic material (e.g. gold and chromium). Since the membrane is nearly acoustically transparent, waves are allowed to propagate through the film, and a small, typically 0.2 - 1.0 mm diameter, active area at the middle of the membrane converts the acoustic displacements into the measurable electric signal. Development and structures of membrane hydrophones are discussed in detail in [4].

Other hydrophone designs include, for example, the ellipsoidal hydrophones [5] and hydrophone arrays [6]. In the ellipsoidal hydrophones, the PVDF membrane is bonded to and backed by the end of an epoxy ellipsoid. The front end of the device is shielded electrically by a thin layer of gold. A typical size of the active element in the ellipsoidal hydrophones is 85-400 μm. A hydrophone array consists of a PVDF film of which small diameter circular regions (a typical diameter is 0.2 mm) have electrical connections. These active regions can generate individually measurable signals. The size, shape, number and spacing of the active elements can vary between different array configurations.

An assumption in acoustic measurements is that the hydrophone does not alter the acoustic field. In practice, however, it is known that in the case of continuous wave (CW) sources, standing waves can be formed between the hydrophone and surrounding structures and may disturb the measurements (see [7] and [2]). Although this phenomenon has been know for a long time, little effort has been made to study it either experimentally or theoretically. The effect of the PVDF membrane hydrophone positioned at different distances from the transducer source operating in CW mode, to the field behind the membrane was examined experimentally in [8]. The transducer was driven at 2.0 - 2.25 MHz which resulted in

0-10% error to the field behind membrane, depending on the hydrophone-transducer separation. The most notable error was observed when the separation was less than 1.5 times the near-field distance. In [9] reflection of a wave pulse from a PVDF membrane was studied in two spatial dimensions using a nonlinear pseudospectral method and simulation results were compared with experimental measurements.

The aim of this study was twofold. Firstly, to computationally determine the effect of the hydrophone on the acoustics field. Five different needle sizes and one membrane hydrophone were used in the simulations. The frequency of the wave field used in this study, varied from 0.5 MHz to 5.0 MHz. In addition, the effect of the backing material with two different needle hydrophone configurations was also compared. Secondly, simulated measurements were used to examine how the reflected waves alter the signal of the hydrophones. This part of the study was carried out for one needle and one membrane hydrophone.

II. COMPUTATIONAL MODEL

To model acoustic interaction of the CW acoustic field and a hydrophone, several assumptions have been made. Firstly, the intensity of the acoustic field was assumed to be so low that nonlinear effects on the wave field could be ignored. Secondly, although PVDF is a solid material and hence capable of bearing shear forces, it was assumed that waves other than dilatational ones could be ignored. This assumption is justified since, due to the geometry of our simulation arrangement, the waves hit the PVDF film in an almost normal direction leading to relatively weak mode shear coupling. Additional approximations associated with the sound source and hydrophones are discussed in Section II-B.

A. The Helmholtz equation and its numerical approximation

Propagation and scattering of linear acoustic waves in a heterogeneous fluid is characterized by the wave equation

$$\nabla \cdot \left(\frac{1}{\rho} \nabla P \right) - \frac{1}{\rho c^2} \frac{\partial^2 P}{\partial t^2} = 0 \tag{1}$$

where P is acoustic pressure, ρ is density and c is the speed of sound. In the case of continuous-waves the field behaves time-harmonically, i.e. $P(r,t) = p(r)e^{-i\omega t}$, where $r = r(x,y,z)$ is the spatial variable. The space-dependent part of the pressure $p(r)$ field can be obtained as the solution of the inhomogeneous Helmholtz equation

$$\nabla \cdot \left(\frac{1}{\rho} \nabla p \right) + \frac{\kappa^2}{\rho} p = 0, \tag{2}$$

with wave number $\kappa = 2\pi f/c + i\alpha$ and where f is the frequency of the wave field and α is the absorption coefficient.

Numerical approximation of the Helmholtz problem in heterogeneous media and in general three dimensional geometry is difficult since the computational complexity increases rapidly with the wave number. In the standard methods, such as the finite difference (FD) and finite element (FE) methods, approximately ten discretization points per wave length are needed to obtain a tolerable accuracy [10]. On the other hand, the use of a time domain method, such as the finite difference time domain (FDTD) method, for CW problems requires a large number of time steps which also leads to heavy computational burden [11]. Various improved methods have been proposed, these include, for example, pseudospectral [12] and k-space methods [13].

Methods that incorporate *a priori* information about the solution to the approximation space (e.g. the partition of unity finite element (PUFEM) [14] and the ultra weak variational formulation (UWVF) [15]) are other promising candidates for reducing the computational burden (see e.g. [16] and [17]).

The computational model used in this study is based on the numerical solution of the Helmholtz problem (2) by the ultra weak variational formulation. For the UWVF the original inhomogeneous Helmholtz problem is decomposed into a finite number of homogeneous subproblems which are coupled with coupled transmission conditions. For each subproblem the field is approximated as a weighted sum of plane waves. In practice, to partition the problem, the method utilizes standard finite element meshes and hence conserves the ability of finite elements to approximate complex three dimensional geometries. The mesh size in the UWVF, however, can be significantly larger than in the FE method, which reduces the time required for mesh generation. The number of plane waves used to approximate the field in a single element depends on the element size and the wave number within the element. The method is discussed in greater detail in the Appendix.

B. Model for the source and the hydrophone

The computation domain used in the simulations was a cylinder whose size varied with the frequency used in the simulations. In the needle hydrophone simulations, the acoustic field was investigated using frequencies from 0.5 MHz to 5.0 MHz. This frequency span is typical for ultrasound therapy [18].

The corresponding radius and length of the cylinder, R and L, respectively, and the radius of the source R_S of the computation domain for different frequencies f are listed in Table I. The radius of the source for each frequency corresponds to 5 wavelengths of the wave field in water. The source of this size is assumed to be sufficient to significantly back-scatter waves hitting to face of the source. The size of the computation domain is limited by reasonable computation time.

[Table 1 about here.]

The source was modeled as a circular domain at the end of the cylinder. In all simulations the source was modelled as an uniformly oscillating surface on which the normal derivative of pressure is

$$\frac{\partial p}{\partial \nu} = i\omega\rho v_n \tag{3}$$

where $\omega = 2\pi f$ is the angular frequency and v_n is the normal velocity of the surface. Depending on the type of hydrophone, a needle or a membrane was embedded in the domain, (Fig. 1). The material properties used in this study for the PVDF are $c = 2200$ m/s, $\rho = 1780$ kg/m^3 and $\alpha = 157$ Np/m/MHz. These are in agreement with the values obtained in experimental measurements and used in other theoretical hydrophone studies (see e.g [19] and [20]). The material surrounding the hydrophone was water with $c = 1500$ m/s, $\rho = 1000$ kg/m^3 and $\alpha = 0$ Np/m/MHz.

[Figure 1 about here.]

The needle hydrophone was modelled as a thin cylinder with diameter D_N. On the tip of the needle hydrophone a 9 μm thick cylindrical domain with diameter D_F modeled the PVDF film. Detailed geometry of the tip of the needle is shown in Fig. 2.

Five different needle hydrophones were studied. The needle and the PVDF film diameters for the hydrophones are shown in Table II. The dimensions of needle and film of hydrophones 1-4 are typical for currently commercially available hydrophones. The dimensions of hydrophone 5, not including the thickness of the PVDF film, are 5 times of those for hydrophone 1. These two hydrophones were used to study the scalability of field anomalies with ratio of the wavelength and needle diameter.

[Table 2 about here.]

[Figure 2 about here.]

The needle, not including the PVDF film, was assumed to be perfectly rigid. Hence, on the surface of the needle the normal derivative of the pressure is zero, i.e.

$$\frac{\partial p}{\partial \nu} = 0. \tag{4}$$

The assumption about the perfectly rigid needle is valid since the surface of the needle is usually made of steel or brass, which have at least 20 times higher acoustic impedances than water.

The backing material behind the PVDF film was in most cases assumed to be absorbing. An absorbing boundary condition for the inner surface of the film can be written as

$$\frac{\partial p}{\partial \nu} - i\mathrm{Re}(\kappa)p = 0. \tag{5}$$

The absorbing backing material can be considered an ideal case. In practice, part of the wave is reflected from the interface between the film and the backing. However, the backing materials vary between different hydrophone configurations.

To evaluate the effect of backing material on the field reflected by the hydrophone, the boundary condition (4) behind the film was also considered. This corresponds to the case in which the film is mounted on the surface of a material with significantly higher acoustic impedance (e.g. steel or copper). Compared to absorbing backing, this configuration provides another end of the scale for backing materials since the wave is completely reflected from the inner end of the film. Hence, most backing materials used in hydrophones lie somewhere between the absorbing and the perfectly rigid assumptions, allowing us to characterize the scale of reflections from the film among many possible backing configurations.

Although in this study the impenetrable needle surface (4) was assumed and the field inside the backing material was ignored, it is possible, in practice, that elastic waves can be generated in the needle hydrophone. For example, it was shown in [21] that surface elastic waves can be induced on a brass backing behind a PVDF film. However, the piece of brass used in that study was significantly larger ($D_N = 50$ mm) than the needles in the present study. On the other hand, the results in [21] suggested that the leaky waves, originating from the surface waves, had only a minor effect compared to reflected and diffracted waves.

The membrane hydrophone was modelled as a single homogeneous 25 μm thick layer of PVDF. To simplify the simulations (and to enable the generation of the tetrahedral mesh), the nonpiezo-material layers were not included in the model. The simulations for the membrane hydrophone were computed for the frequencies of 1.0 MHz and 2.0 MHz. The geometric parameters for the mesh at 1.0 MHz were $R = 12.5$ mm, $L = 30.0$ mm and $R_S = 7.5$ mm. In the case of 2.0 MHz source, they were $R = 6.25$ mm, $L = 20.0$ mm and $R_S = 3.75$ mm. Frequencies around 1.0 MHz are of particular interest in the ultrasound therapy of brain [22]. Therefore it is vital to understand possible measurement errors for this frequency. On the other hand, in [8], experimental measurements using 2.0 MHz sources were done to study errors associated to membrane hydrophone measurements of CW fields. To enable comparison with those, the simulations with 2.0 MHz are also computed. As in the case of the needle hydrophones, the size of the computation domain is limited by reasonable computation time.

To evaluate the signal produced by the hydrophone, an active region with a diameter of 0.50 mm was defined on the surface of the membrane. The signal was obtained by integrating the pressure field over this active area. The electric signal generated by a hydrophone is proportional to the pressure on the front face of the membrane [20].

The simulated hydrophone measurement for both needle and membrane hydrophone was carried out in three steps. First, a computation mesh with the hydrophone at the desired location was generated. Second, the UWVF approximation of the field was computed. And third, the signal for the hydrophone was obtained by integrating the UWVF approximation over the front face of the PVDF film.

To decrease spurious numerical reflections from the exterior boundary, the absorbing boundary condition (5) was used on those parts of the exterior boundary which were not modelled as the source or rigid surface.

Computation meshes for the problem were generated with the mesh generator of the FEMLAB2.2 (COMSOL, Inc. Burlington, MA) finite element package. Typical meshes used in the simulations are shown in Fig. 3. Depending on the simulation, the number of elements in the mesh was between 35 000 and 80 000. Due to the requirement of detailed geometry of the hydrophones, the element size within a mesh varied considerably. Consequently, the number of basis functions for a single element in the UWVF scheme varied between 1 and 130.

[Figure 3 about here.]

III. RESULTS

A. Needle hydrophones

1) Distortion in the field: The effect of the needle hydrophone on the field under measurement was studied by comparing simulated pressure fields in the absence and presence of the hydrophone. The overall fields (i.e the fields with and without a hydrophone) are normalized to the maximum value of the field without a hydrophone in the region shown. In the results section, the fields with and without hydrophone are referred to as p and p_w, respectively. To study the distortion caused by the hydrophone, the difference field $p_w - p$ is also presented. To show what portion of the incident field reflects from the tip, the difference field $p_w - p$ was normalized to the amplitude of the incident field at the location of the tip.

The field scattered by a needle hydrophone was studied as a function of distance from the tip of the needle to the source d. Pressure amplitude distributions are shown for hydrophone 4 with $D_N = 1.47$ mm and the frequency $f = 0.5$ MHz in Fig. 4. The distance d varied from 10 to 30 mm. Corresponding difference fields along the acoustic axis of the source are presented in Fig. 5.

[Figure 4 about here.]

A notable pattern of standing waves can be seen in all three cases, although the amplitude of the waves diminishes with the increasing distance between the hydrophone's effective element and the surface of the radiating source.

[Figure 5 about here.]

The effect of needle diameter on the field distortion for fixed frequency $f = 1.0$ MHz and needle distance $d = 10$ mm were studied as a function of the hydrophone size. The pressure amplitude fields in Fig. 6 show that only the thickest hydrophone causes significant distortion. It is noteworthy that the diameter of the hydrophone 4 ($D_N = 1.47$ mm) was almost equal to the wavelength ($\lambda = 1.5$ mm) of the field. The plot along the acoustic axis in Fig. 7 confirms that the two thinnest needles have only a negligible effect on the field between the needle and the source.

[Figure 6 about here.]

[Figure 7 about here.]

The pressure amplitude fields for hydrophone 3 with $D_N = 0.46$ mm at a distance of $d = 10$ mm for different frequencies are shown in Fig. 8. Note the increase in the amplitude of the difference field with frequency between the source and the needle. The difference fields on the acoustic axis are presented in Fig. 9.

[Figure 8 about here.]

[Figure 9 about here.]

2) Effect of the backing material: Two hydrophone configurations with absorbing and rigid backing materials were compared in Fig. 10. The pressure fields are computed for the frequency $f = 1.0$ MHz and hydrophone 4. The distance between the tip of the needle and the source was $d = 20$ mm.

[Figure 10 about here.]

[Figure 11 about here.]

3) Simulated hydrophone measurement: The measurement for hydrophone 4 ($D_N = 1.47$ mm) and the frequency $f = 0.5$ MHz was simulated. The hydrophone was scanned along the acoustic axis of the source.

A comparison between a simulated measurements with an ideal hydrophone and with a real hydrophone are shown in Fig. 12. The ideal hydrophone measurement shows the pointwise value of the pressure field without a hydrophone. The fields are normed the mean pressure amplitude in the shown axis.

[Figure 12 about here.]

4) Scalability of the simulated anomalies for higher frequencies: The difference fields $p_w - p$ for the frequencies 1.0 MHz and 5.0 MHz are shown in Fig. 13. In the case of $f = 1.0$ MHz field, hydrophone 5 ($D_N = 1.5$ mm, $D_F = 0.2$ mm) located at the distance $d = 25$ mm. The second simulation was computed at the frequency $f = 5.0$ MHz with hydrophone 1 ($D_N = 0.3$ mm, $D_F = 0.04$) mm) at the distance $d = 5$ mm. In both simulations all dimensions, not including the thickness of the PVDF film (9μm), were equal with respect to the wavelength of the field. The wavelengths were $\lambda = 1.5$ mm and $\lambda = 0.3$ mm for 1.0 MHz and 5.0 MHz, respectively. The relative difference of these two fields was 2.0 %.

[Figure 13 about here.]

B. Membrane hydrophone

1) Distortion in the field: The membrane hydrophone simulations in this study were limited to frequencies $f = 1.0$ MHz and $f = 2.0$ MHz. Similarly to the needle hydrophone studies, all results shown are normalized, however, now with the maximum amplitude in water in the absence of the membrane. The effect of the membrane at a distance $d = 20$ mm from the 1.0 MHz source is shown in Fig. 14. An observable standing wave field is generated between the source and the membrane. This can been seen more clearly from the plot along the acoustic axis of the source (Fig. 15).

[Figure 14 about here.]

[Figure 15 about here.]

A similar periodic anomaly is shown in the 2.0 MHz field (Figs. 16 and 17). The membrane was located at the distance of $d = 10$ mm.

[Figure 16 about here.]

[Figure 17 about here.]

2) Simulated hydrophone measurement: To evaluate how reflections from the membrane distort the signal of the hydrophone, the measurement of the membrane hydrophone was simulated for the frequencies $f = 1.0$ MHz and $f = 2.0$ MHz. The 1.0 MHz field was measured on the acoustic axis of the source from distances of 10 - 20 mm with 0.25 mm spacing. The simulation procedure was similar to that used for the needle hydrophone and the results are shown in Fig. 18.

The averaged simulated measurement is compared with the the field without the membrane in Fig. 19. The field at each point was averaged with two adjacent points.

[Figure 18 about here.]

[Figure 19 about here.]

Finally, the simulated membrane hydrophone scan along the acoustic axis of the 2.0 MHz source from 10.0 to 15.0 mm with 0.1 mm spacing is shown in Fig. 20. Furthermore, Fig. 21 shows the relative error in the pressure amplitude at the point 18 mm from the transducer as a function of the location of the scanning membrane hydrophone. The distance from the transducer to the hydrophone is divided by the near-field distance 18.56 mm. The relative error in the pressure amplitude is shown compared to the value of the field at the same point without the hydrophone. The error is shown also in comparison to the mean value of the field at different transducer-hydrophone separations. The measured error presented in the same figure is extracted from Figure 12 of [8].

[Figure 20 about here.]

[Figure 21 about here.]

IV. DISCUSSION

In this study the three-dimensional ultra weak variational formulation (UWVF) was used for analyzing distortions in continuous-wave fields caused by needle- and membrane hydrophones. Furthermore, simulated measurements for the hydrophones were computed. The frequency span of the simulations was 0.5 - 5.0 MHz which is typical for the ultrasound therapy. In many therapeutic applications of ultrasound continuous-waves are used and therefore it is essential to understand possible anomalies related to the pressure field measurements.

In addition to the modelling approximations, the numerical procedure used in this study has two main sources of error. First, by limiting the study to the relatively small computation domain and by using the approximate absorbing boundary condition (5) on the exterior boundary of the domain, minor spurious numerical reflections of the waves are generated from the boundary into the cylinder. The reflections originate mainly from the incident field of the source. Therefore, they are eliminated from the difference field $p_w - p$, Second, as all numerical methods for the Helmholtz equation, the UWVF has a limited numerical accuracy which for problems studied here, means an error of the order 0.1-1.0 %. This estimate of the accuracy was obtained by comparing two solutions for the same geometry and frequency, computed in different meshes. In both cases, the method for choosing the number of basis functions was the same as described in the Appendix. Computation time for the a single wave field in this study varied from 1500 to 3000 seconds.

For needle hydrophones, the major distortion in continuous-wave measurements is most likely due to the back-scattered waves from the tip of the hydrophone. Some of these waves interfere with the incident field. Standing wave patterns are formed between the needle and the source element (or a structure between the needle and the source). Obviously, the amplitude of the field reflected from the tip of the hydrophone is proportional to the amplitude of the incident field at the measurement point (i.e. at the location of the tip).

The distortion as a function of the frequency was investigated (Fig. 8). For the highest frequency ($f = 2.0$ MHz), the tip of the needle was located near a local near-field minimum. In comparison to the maximum amplitude of the field, this resulted in a relatively weak reflected wave. Since the difference fields were normed with the value of the incident field at the tip, due to limited accuracy of the UWVF approximation, the weak difference field is shown as somewhat noisy.

The results for the needle hydrophones suggested that scattering from the tip of the needle became observable when the diameter of the needle was over half of the wavelength. Although a notable standing wave field was observed for the frequency $f = 0.5$ MHz and hydrophone 4 at the distance $d = 10$ mm in Fig. 4, the simulated measurement with the same hydrophone in Fig. 12 closely follows the profile of the field at the acoustic axis. Therefore, for the needle hydrophones it is not evident that the difference in the field and the measurement was only due to standing waves between the needle and the source, in particular, since the discrepancy did not have the same clear periodic structure as was observed in the simulated measurement for the membrane hydrophone. Other possible sources of error in measurements include, for example, the diffraction effects that are studied in detail in [23]. The diffraction effects emerge since the hydrophone with the finite size active film is used to measure the “point” value of the acoustic field.

To study the effect of the backing material behind the PVDF film on the field anomalies, a comparison between rigid and absorbing backing materials was simulated (Fig.11). It was observed that the amplitude of the standing wave pattern with the rigid backing was about 50 percent higher than that of the absorbing material.

Although the main part of the needle hydrophone simulations was computed for the frequencies 0.5 - 2.0 MHz, scalability of the results for higher frequencies was also investigated. Simulations with frequencies

1.0 MHz and 5.0 MHz showed that anomalies in the field are scalable with respect to the ratio of the wavelength and the needle (and PVDF film) diameter. In very high frequencies, however, the scalability can be expected to fail due to the thickness resonant frequencies of the film.

In the case membrane hydrophones, both the field between the transducer and the membrane; and the simulated signal of the hydrophone revealed a half wavelength periodic distortion in comparison to the field without the membrane. The relative amplitude of the disturbance was about 20%. For the 2.0 MHz transducer, the field at a fixed distance from the source behind the membrane hydrophone was simulated. This case imitates the experimental measurements performed in [8]. The relative error of the field in simulations was 0-30 % when compared with the pressure amplitude at the same spot without the hydrophone. The error in comparison to the mean value of the field at the same point at different transducer-hydrophone separations was 0-20 %. In [8], under 10% errors were observed by using a second membrane hydrophone at a fixed distance from the transducer. Hence, the model seems to predict the magnitude of the error reasonably well although the simulated errors were slightly over estimated in comparison to the experimental measurements.

The difference between the simulations and experimental measurements has several possible reason. For example, the model used in this study did not include the changes in the output of the source due to the standing waves [24]. And the second membrane used to measure errors in [8], interacts also with the wave field and therefore may cause additional anomalies.

As discussed in [7], a slight rotation of the hydrophone can eliminate the standing waves, causing nonoverlapping reflected and main beams. Alternatively, in this study, an averaging technique was used to reduce the amplitude of the distortion. To do this, the field at a given measurement point was averaged with two adjacent points. As shown in Figs. 18 and 19 the benefit of the averaging is evident, but one must bear in mind that the procedure may also lose other fine structures from the field.

The simulations were computed only for a planar circular source. Since the amplitude of the scattering from the hydrophone is proportional to the amplitude of the field at location of hydrophone, it is obvious that strong distortion may result in, when focused CW fields are measured near the focal spot. In addition, this study was limited only region near the hydrophone (i.e only part of the needle or membrane was considered) which naturally eliminates possible standing waves from surrounding structures (e.g. from the walls of the measurement tank and holder of the hydrophone).

The study was limited only a relatively small number of hydrophones and a simplified hydrophone model was used. An improved model could include the elastic properties of the hydrophones, multilayered structures and electric characteristic of the PDVF film. These have been used in one dimensional modelling of the membrane hydrophones [20]. Alternatively, an aim of this study was to include more detailed characterization of the incident fields and hydrophone geometries. To limit the extend of the study, the simulations were computed only for the needle and membrane hydrophones. However, a similar simulations should be possible also for the ellipsoidal or array hydrophones.

ACKNOWLEDGMENT

This study was supported by Finnish Academy Grants 72431, 80773 and 200627; and by grants to Tomi Huttunen from the Saastamoinen Foundation and the Finnish Cultural Foundation of northern Savo.

APPENDIX

The ultra weak variational formulation (UWVF)

For the UWVF the computational domain Ω is partitioned into a finite number of subdomains Ω_j, $1 \leq j \leq K$ (standard tetrahedral finite element meshes are used in this study, see Fig. 3). Let us denote by ν_j the outward unit normal for the j'th element. The boundary between elements Ω_j and Ω_ℓ is denoted by $\Sigma_{j,\ell}$. Furthermore, if the element Ω_j is on the boundary of domain Ω, the coinciding boundary is denoted by $\partial\Omega_j \cap \partial\Omega = \Gamma_j$.

Assuming that the material parameters ρ and c are approximated with piecewise constant functions, the Helmholtz problem (2) can be decomposed for all $1 \leq j \leq K$ as

$$\Delta p_j + \kappa_j^2 p_j = 0 \text{ in } \Omega_j \tag{6}$$

where $p_j = p|_{\Omega_j}$. The subproblems (6) are connected across the element interfaces $\Sigma_{j,\ell}$ with the coupled boundary condition

$$\frac{1}{\rho_j}\frac{\partial p_j}{\partial \nu_j} - i\sigma p_j = -\frac{1}{\rho_\ell}\frac{\partial p_\ell}{\partial \nu_\ell} - i\sigma p_\ell. \tag{7}$$

Physically it can be considered as a coupled form of the transmission conditions which characterize the continuity of the pressure and the normal particle velocity across the interface [25]. The coupling parameter σ is obtained as the mean value of $\text{Re}(\kappa)/c$ over the interface

$$\sigma = \frac{1}{2}\left(\frac{\text{Re}(\kappa_j)}{\rho_j} + \frac{\text{Re}(\kappa_\ell)}{\rho_\ell}\right) \quad \text{on } \Sigma_{j,\ell}. \tag{8}$$

On the exterior boundaries Γ_j the boundary condition is given in the form

$$\left(\frac{1}{\rho_j}\frac{\partial p_j}{\partial \nu_j} - i\sigma p_j\right) = \tau\left(-\frac{1}{\rho_j}\frac{\partial p_j}{\partial \nu_j} - i\sigma p_j\right) + g \tag{9}$$

where $\tau \in \mathbb{C}$, $|\tau| \leq 1$, and the coupling parameter $\sigma > 0$, $\sigma \in \mathbb{R}$. The source term is denoted by g.

The type of boundary condition on the exterior boundary for the problem can be adjusted with the parameters τ, σ and g. The implementations of the exterior boundary conditions (3), (4) and (5) in the UWVF scheme are summarized in Table III. A requested boundary condition is obtained by choosing the listed parameters for Equation (9).

[Table 3 about here.]

Now define the function f, $f|_{\partial\Omega_j} = f_j$ on the element boundaries as follows

$$f_j = \left(\left(-\frac{1}{\rho_j}\frac{\partial}{\partial\nu_j} - i\sigma\right)p_j\right)\Bigg|_{\partial\Omega_j}, \quad 1 \leq j \leq K. \tag{10}$$

In [15] Cessenat and Despres show that f_j satisfies *the ultra weak variational formulation*

$$\sum_{j=1}^{K}\int_{\partial\Omega_j}\frac{1}{\sigma}f_j\overline{\left(-\frac{1}{\rho_j}\frac{\partial}{\partial\nu_j} - i\sigma\right)q_j} \quad - \tag{11}$$

$$\sum_{j=1}^{K}\sum_{\ell=1}^{K}\int_{\Sigma_{j,\ell}}\frac{1}{\sigma}f_\ell\overline{\left(\frac{1}{\rho_j}\frac{\partial}{\partial\nu_j} - i\sigma\right)q_j} \quad +$$

$$\sum_{j=1}^{K}\int_{\Gamma_j}\frac{\tau}{\sigma}f_j\overline{\left(\frac{1}{\rho_j}\frac{\partial}{\partial\nu_j} - i\sigma\right)q_j} \quad =$$

$$\sum_{j=1}^{K}\int_{\Gamma_j}\frac{1}{\sigma}g\overline{\left(\frac{1}{\rho_j}\frac{\partial}{\partial\nu_j} - i\sigma\right)q_j} \tag{12}$$

for all test functions q_j which are the solutions of the adjoint Helmholtz equation

$$\Delta\overline{q}_j + \kappa_j^2\overline{q}_j = 0 \quad \text{in } \Omega_j, \tag{13}$$

where the overbar denotes complex conjugation.

A discrete form of the UWVF (10) is obtained by approximating the function f_j on a plane wave basis as follows

$$f_j^a = \sum_{n=1}^{N_j} f_{j,n}\left(-\frac{1}{\rho_j}\frac{\partial}{\partial\nu_j} - i\sigma\right)\varphi_{j,n} \tag{14}$$

where

$$\varphi_{j,n} = \begin{cases} \exp(i\overline{\kappa}_j d_{j,n}\cdot r) & \text{in } \Omega_j \\ 0 & \text{elsewhere.} \end{cases} \tag{15}$$

The directions $d_{j,n}$ are chosen according to optimized spherical covering for a unit sphere [26]. In addition, set $q_j = \varphi_{j,n}$, $n = 1, \ldots, N_j$. This leads to the matrix equation [15]

$$(I - D^{-1}C)X = D^{-1}b. \tag{16}$$

from which the unknowns $X = (f_{1,1}, \ldots, f_{1,N_1}, \ldots, f_{K,N_K})^T$ can be computed. As proposed in [16], the matrix equation (16) is solved with the iterative stabilized bi-conjugate gradient solver [27].

The matrices D and C are sparse block matrices. In particular, the matrix D is a Hermitian block diagonal matrix consisting of the K blocks $D_j \in \mathbb{C}^{N_j \times N_j}$. It is shown [16] that the condition number of the blocks D_j can be used to predict a stable number of basis functions N_j for each element. Using the dynamical procedure for choosing N_j, the maximum allowed condition number in this study was set to $5 \cdot 10^5$. However, if this did not result in convergent bi-conjugate gradient iteration, the condition number was lowered to $1 \cdot 10^5$.

From Equations (10) and (14) it can be seen that the pressure on the element boundaries can be approximated as

$$p^a = \sum_{n=1}^{N_j} f_{j,n} \varphi_{j,n} \quad \text{on } \partial\Omega_j. \tag{17}$$

If $\kappa_j \in \mathbb{R}$ the equations (6) and (13) are equal and the approximation (17) is also valid within the element Ω_j. Inside the elements in which $\kappa_j \notin \mathbb{R}$ this approximation is usable, at least if the size of the element is relatively small. In the problem at hand, elements with complex wave numbers were located in the PVDF film causing them to be extremely small.

The parallel UWVF solver was coded with Fortran90 using MPI (Message Passing Interface) for parallelization. The results were computed in a Beowulf PC cluster consisting of 12 1.8 MHz Pentium 4 processors with 1 GB RAM for each processor.

REFERENCES

[1] G. Harris, R. Preston, and A. DeReggi, “The impact of piezoelectric PVDF on medical ultrasound exposure measurements, standards, and requlations,” *IEEE Transactions on Ultrasonics, Ferroelectrics, and Frequency Control*, vol. 47, no. 6, pp. 1321–1335, 2000.

[2] G. Harris, “Hydrophone measurements in diagnostic ultrasound fields,” *IEEE Transactions on Ultrasonics, Ferroelectrics, and Frequency Control*, vol. 35, no. 2, pp. 87–101, 1988.

[3] P. Lewin, “Miniature pezoelectric polymer ultrasonic hydrophone probes,” *Ultrasonics*, vol. 19, no. 5, pp. 213–216, 1981.

[4] S. Robinson, R. Preston, M. Smith, and C. Millar, “PVDF reference hydrophone development in the UK - from fabrication and lamination to use as secondary standards,” *IEEE Transactions on Ultrasonics, Ferroelectrics, and Frequency Control*, vol. 47, no. 6, pp. 1336–1343, 2000.

[5] A. Selfridge and P. Goetz, “Ellipsoidal hydrophone with improved characteristics,” in *IEEE Ultrasonics symposium*, 1999, pp. 1181–1184.

[6] A. Hurrell and F. Duck, “A two-dimensional hydrophone array using piezo-electric PVDF,” *IEEE Transactions on Ultrasonics, Ferroelectrics, and Frequency Control*, vol. 47, no. 6, pp. 1345–1353, 2000.

[7] F. Duck, H. Starritt, and S. Anderson, “A survey of the acoustic output of ultrasonic Doppler equipment,” *Clinical Physics and Physiological Measurement*, vol. 8, no. 1, pp. 39–49, 1987.

[8] R. C. Preston, D. Bacon, A. Livett, and K. Rajendran, “PVDF membrane hydrophone performance properties and their relevance to the measurement of the acoustic output of medical ultrasound equipment,” *Journal of Physics E: Scientific Instrumentation*, vol. 16, pp. 786–796, 1983.

[9] G. Wojcik, T. Szabo, J. Mould, L. Carcione, and F. Clougherty, “Nonlinear pulse calculations and data in water and a tissue mimic,” in *IEEE Ultrasonics symposium proceedings*, 1999, pp. 1521–1526.

[10] F. Ihlenburg, *Finite element analysis of acoustic scattering*. Springer, 1998.

[11] R. Schechter, K. Simmonds, N. Batra, R. Mignogna, and R. Delsanto, “Use of a transient wave propagation code for 3D simulation of cw radiated trasducer fields,” *Ultrasonics*, vol. 37, pp. 89–96, 1999.

[12] G. Wojcik, B. Fornberg, R. Waag, L. Carcione, J. Mould, L. Nikodym, and T. Driscoll, “Pseudospectral methods for large-scale bioacoustic models,” *IEEE Ultrasonics Symposium Proceeding*, vol. 2, pp. 1501–1506, 1997.

[13] T. Mast, L. Souriau, D. Liu, M. Tabei, A. Nachman, and R. Waag, “A k-space method for large-scale models of wave propagation in tissue,” *IEEE Transactions on Ultrasonics, Ferroelectrics, and Frequency Control*, vol. 48, no. 2, pp. 341–354, 2001.

[14] I. Babuška and J. Melenk, “The partition of unity method,” *International Journal for Numerical Methods in Engineering*, vol. 40, pp. 727–758, 1997.

[15] O. Cessenat and B. Despres, “Application of an ultra weak variational formulation of elliptic PDEs to the two-dimensional Helmholtz problem,” *SIAM Journal of Numerical Analysis*, vol. 35, no. 1, pp. 255–299, 1998.

[16] T. Huttunen, P. Monk, and J. Kaipio, “Computational aspects of the ultra-weak variational formulation,” *Journal of Computational Physics*, vol. 182, pp. 27–46, 2002.

[17] O. Laghrouche and P. Bettess, “Short wave modelling using special finite elements,” *Journal of Computational Acoustics*, vol. 8, no. 1, pp. 189–210, 2000.

[18] G. ter Haar, “Therapeutic ultrasound,” *European Journal of Ultrasound*, vol. 9, pp. 3–9, 1999.

[19] P. Bloomfield, W.-J. Lo, and P. Lewin, “Experimental study of the acoustic properties of polymers utilized to construct PVDF ultrasonic transducers and the acousto-electric properties of PVDF and P(VDF/TrEE) films,” *IEEE Transactions on Ultrasonics, Ferroelectrics, and Frequency Control*, vol. 47, no. 6, pp. 1397–1405, 2000.

[20] P. Gélat, R. Preston, and A. Hurrell, “Development, validation and publication of a complete theoretical model for hydrophone/amplifier transfer characteristics,” National Physical Laboratory, Tech. Rep. CMAM 61, 2001.

[21] Y. Nakamura and T. Otani, “Study of surface elastic wave induced on backing material and diffracted field of a piezoelectric polymer film hydrophone,” *The Journal of the Acoustical Society of America*, vol. 94, no. 3, pp. 1191–1199, 1993.

[22] K. Hynynen, “Review of ultrasound therapy,” *IEEE Ultrasonics Symposium*, pp. 1305–1313, 1997.

[23] A. Goldstein, D. Gandhi, and W. O. Jr., “Diffraction effects in hydrophone measurements,” *IEEE Transactions on Ultrasonics, Ferroelectrics, and Frequency Control*, vol. 45, no. 4, pp. 972–979, 1998.

[24] K. Beissner, “The influence of membrane reflections on ultrasonic power measurements,” *Acustica*, vol. 50, pp. 194–200, 1982.

[25] J. Benamou and B. Despres, “A domain decomposition method for the Helmholtz equation and related optimal control problems,” *Journal of Computational Physics*, vol. 136, pp. 68–82, 1997.

[26] R. Hardin, N. Sloane, and W. D. Smith. (1997, May) Spherical converings. [Online]. Available: http://www.research.att.com/ njas/coverings/index.html

[27] H. V. D. Vorst, “Bi-CGStab: A fast and smoothly converging variant of Bi-CG for the solution of nonsymmetric linear systems,” *SIAM Journal Scientific and Statistic Computing*, vol. 13, no. 2, pp. 631–644, 1992.

LIST OF FIGURES

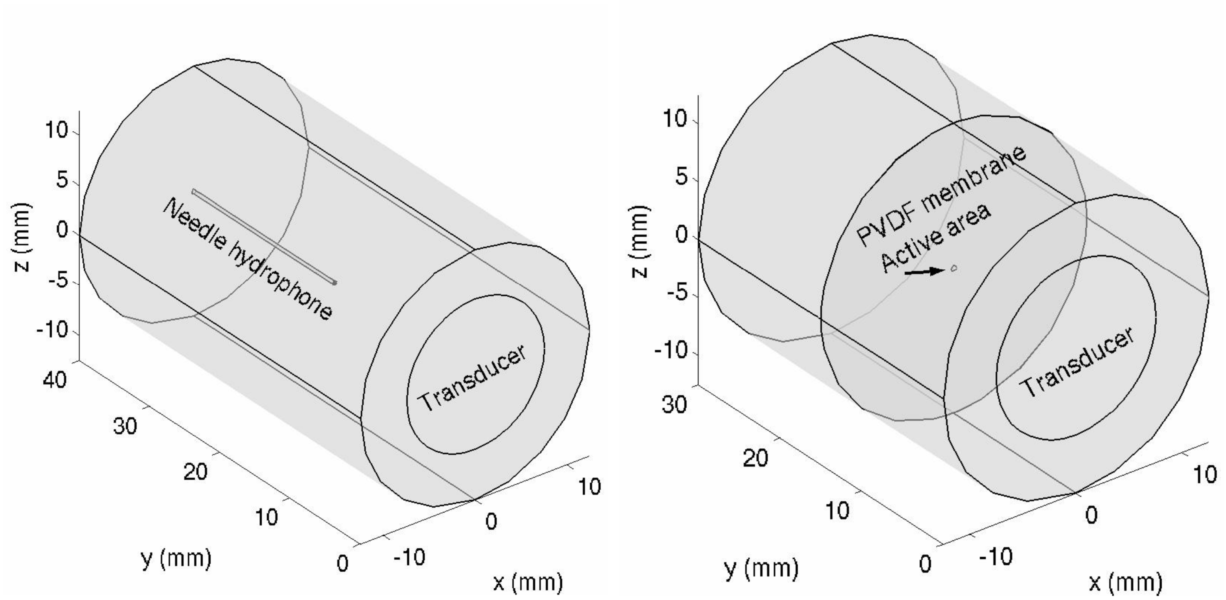

Fig. 1. Geometries of the needle hydrophone (left) and membrane hydrophone (right) simulations. In the simulations the material surrounding hydrophones is water.

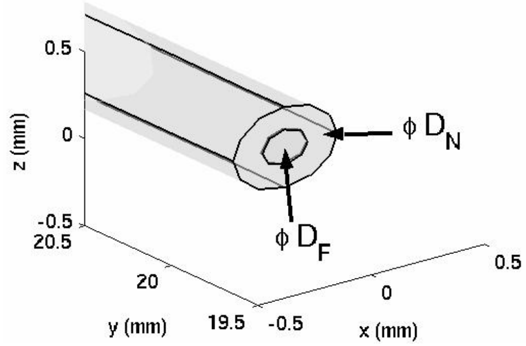

Fig. 2. Detailed geometry of the tip of the needle hydrophone.

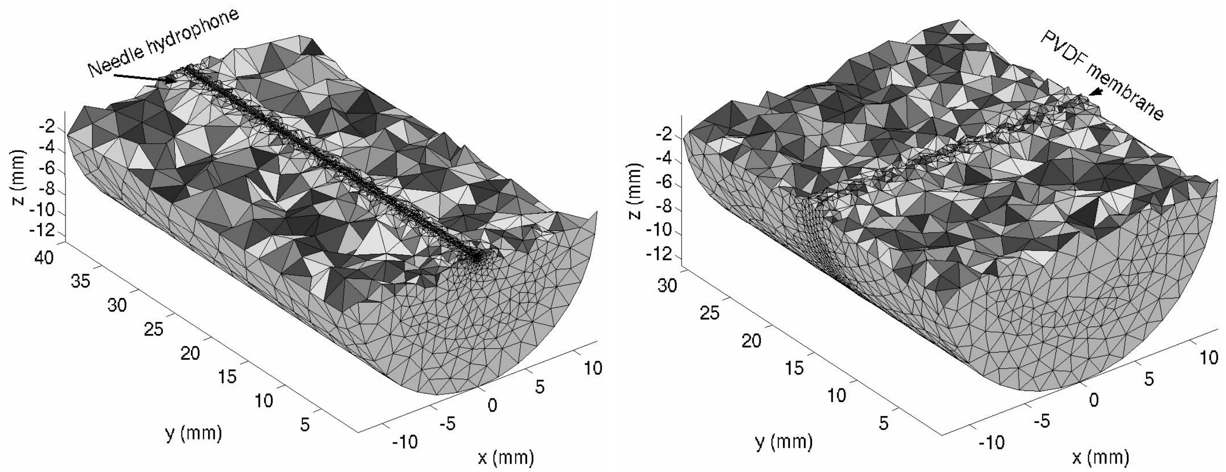

Fig. 3. Cross-sections of typical meshes used in needle hydrophone (left) and membrane hydrophone (right) simulations. To ensure maximal accuracy of the UWVF approximation between the needle and the source, relatively small tetrahedra are used in the mesh between the tip of the needle and the transducer.

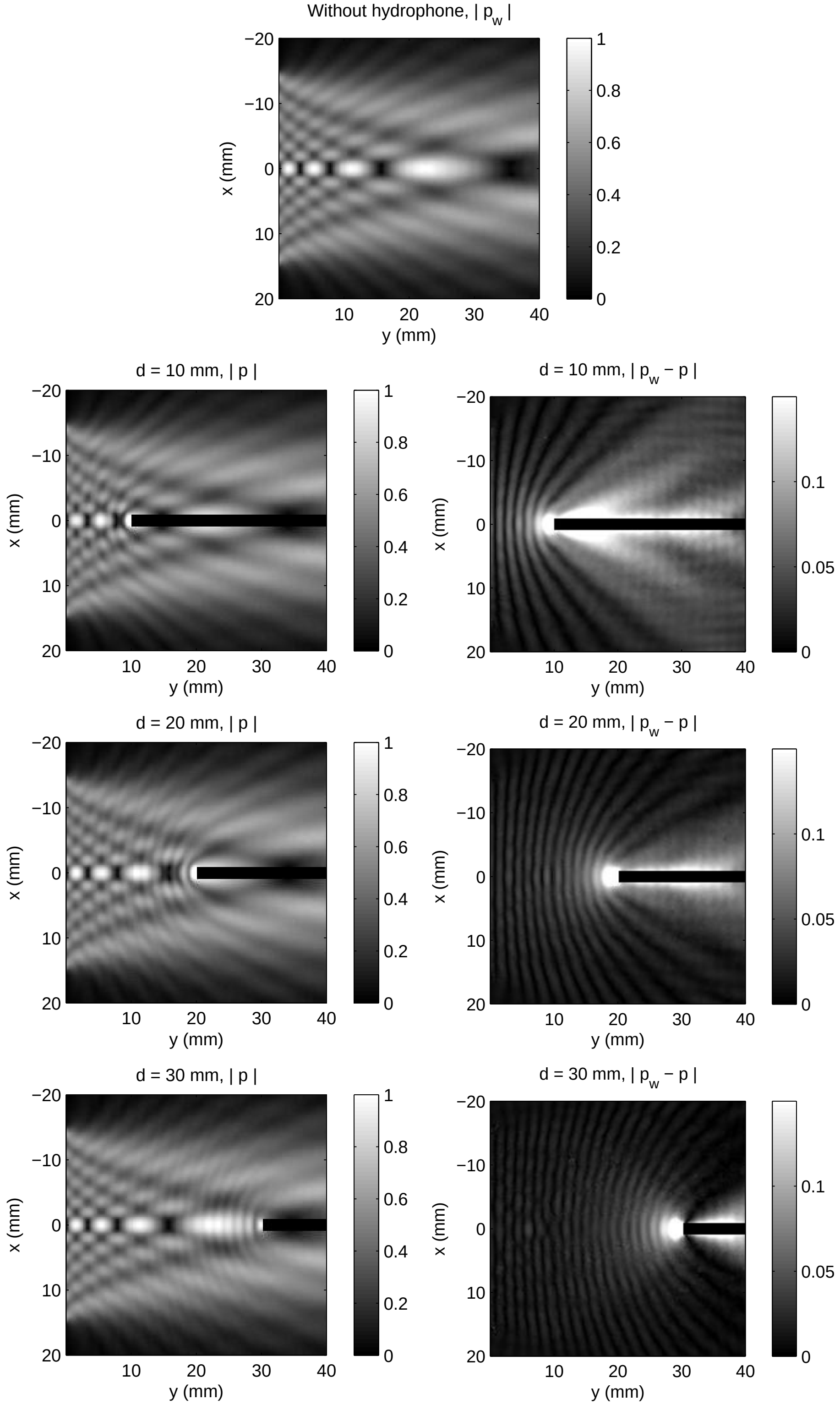

Fig. 4. Scattering from the needle hydrophone 4 with $D_N = 1.47$ mm for different distances d from the source. Left column shows the fields with the hydrophone. Right column presents the difference with the without hydrophone case. The results are computed for the frequency $f = 0.5$ MHz.

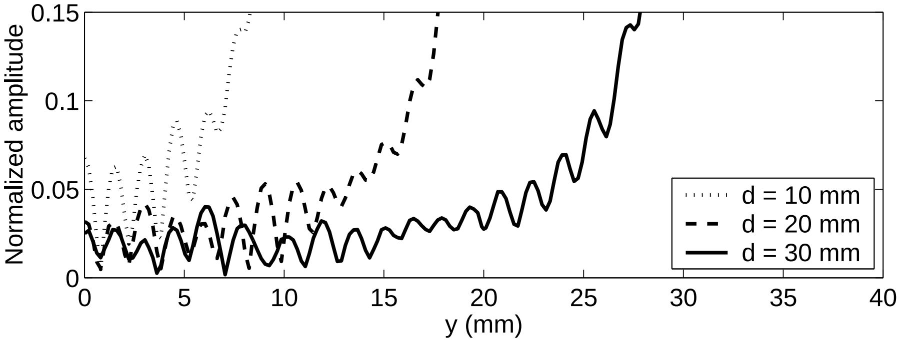

Fig. 5. The difference pressure amplitude fields $|p_w - p|$ along the acoustic axis of the source for different needle - source distances ($f = 0.5$ MHz, $D_N = 1.47$ mm).

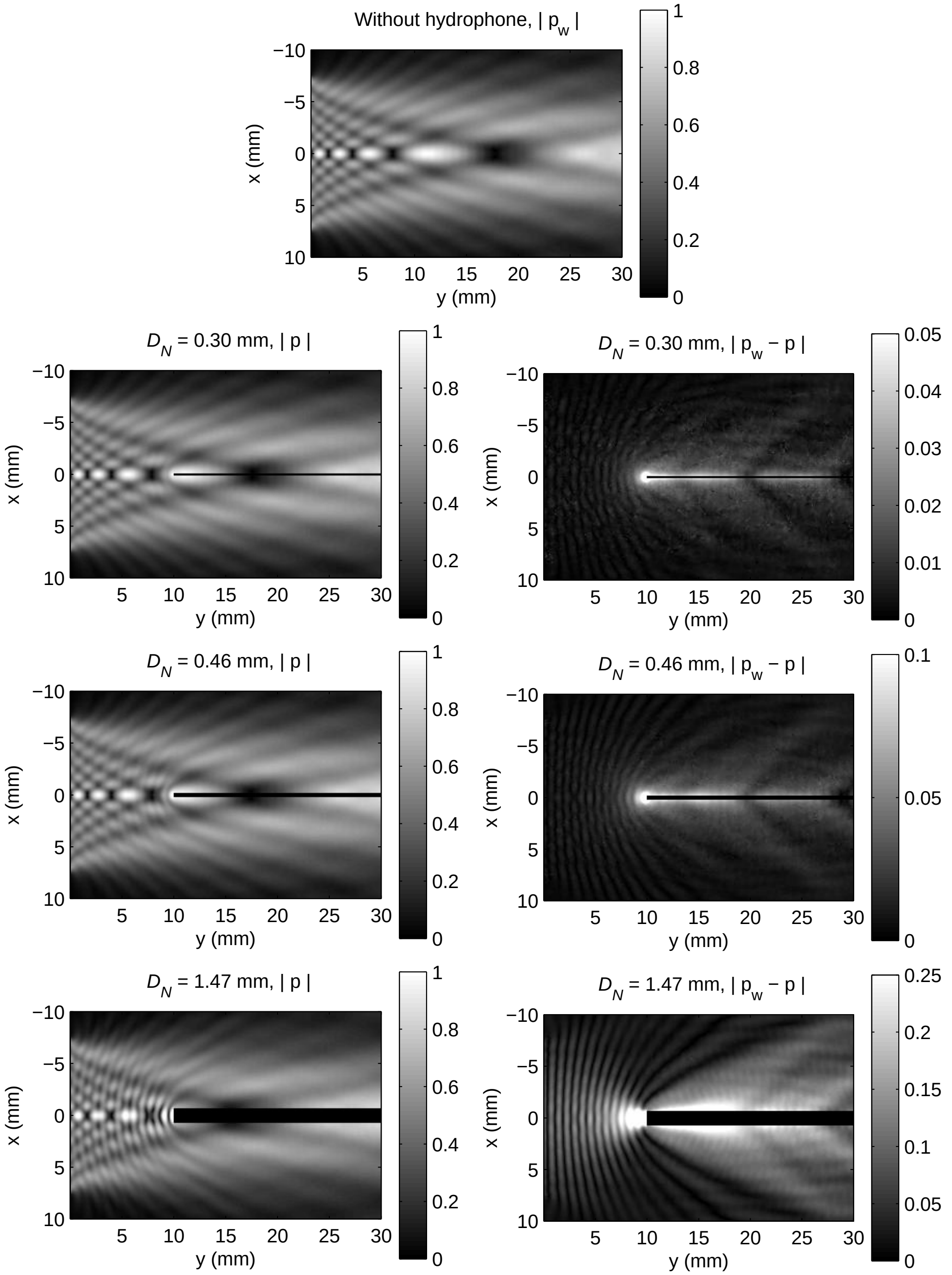

Fig. 6. Effect of the needle diameter D_N to the scattered field. The frequency is $f = 1.0$ MHz and distance from the source to the tip of the needle $d = 10$ mm. Left column shows the field with the hydrophone and right column presents the difference with the without hydrophone case.

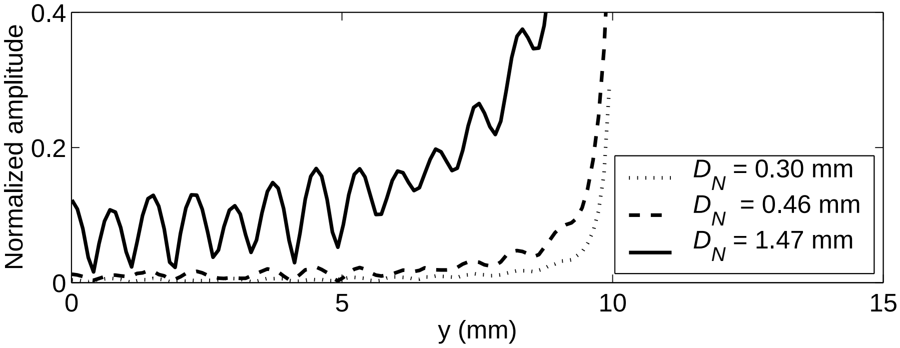

Fig. 7. The difference fields $|p_w - p|$ along the acoustic axis of the source for different needle sizes ($f = 1.0$ MHz, $d = 10$ mm).

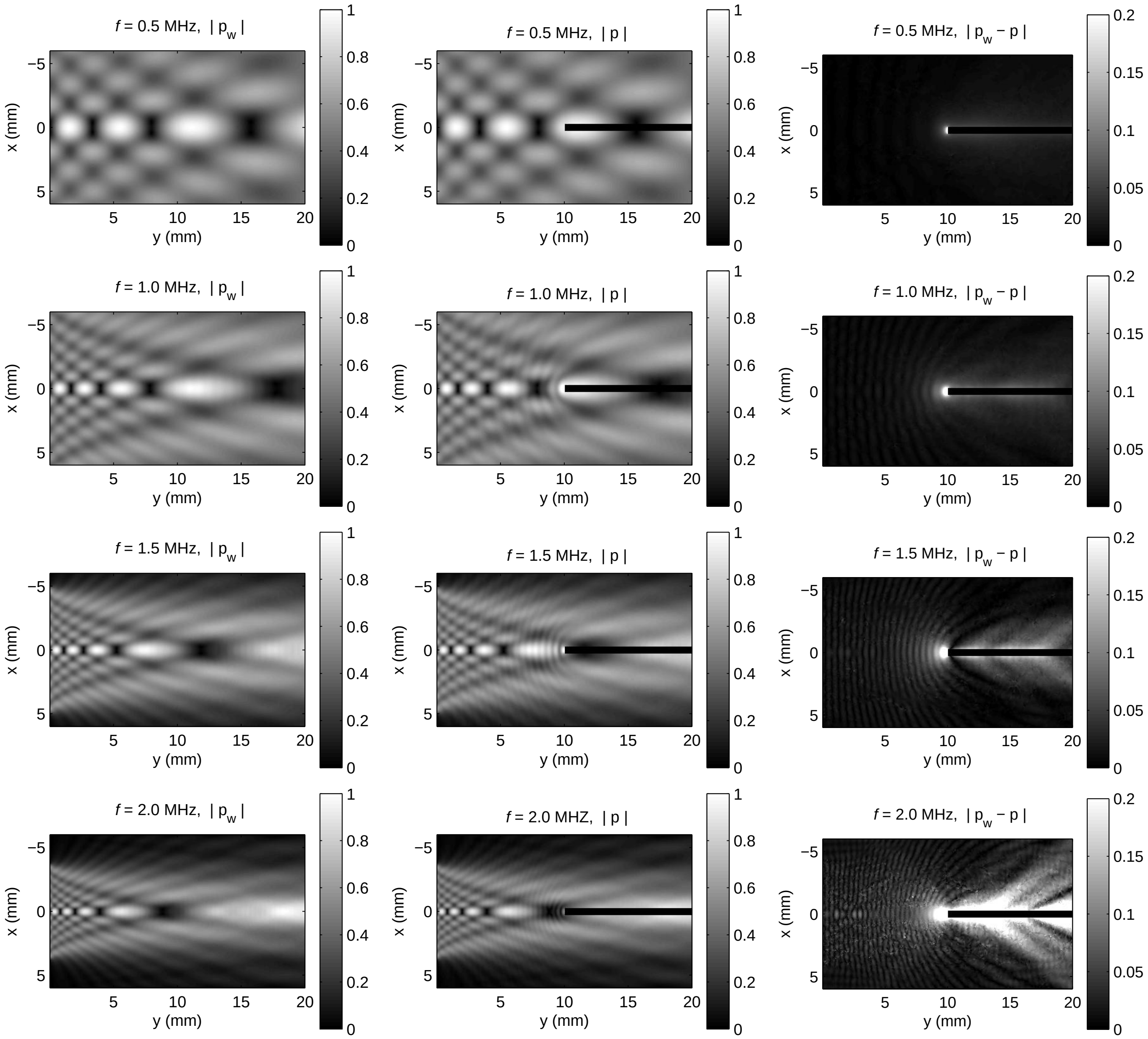

Fig. 8. Effect of frequency to scattering from the needle hydrophone 3 with $D_N = 0.46$ mm. The distance between the source and the tip of the needle is $d = 10$ mm.

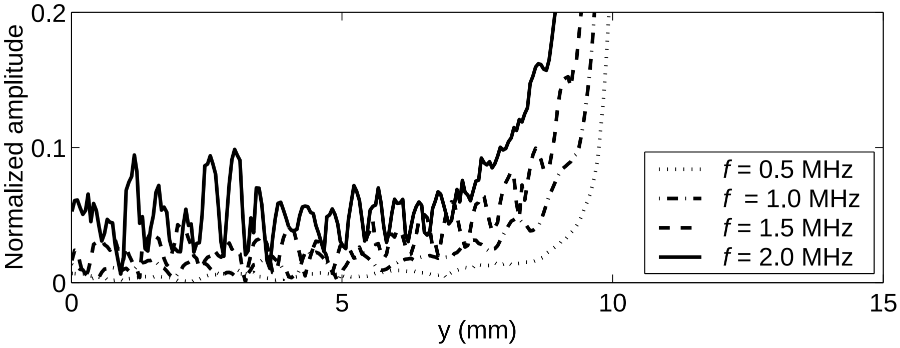

Fig. 9. The difference fields $|p_w - p|$ on the acoustic axis of the source for frequencies $f = 0.5$, 1.0, 1.5 and 2.0 MHz. The distance from source to hydrophone is $d = 10$ mm.

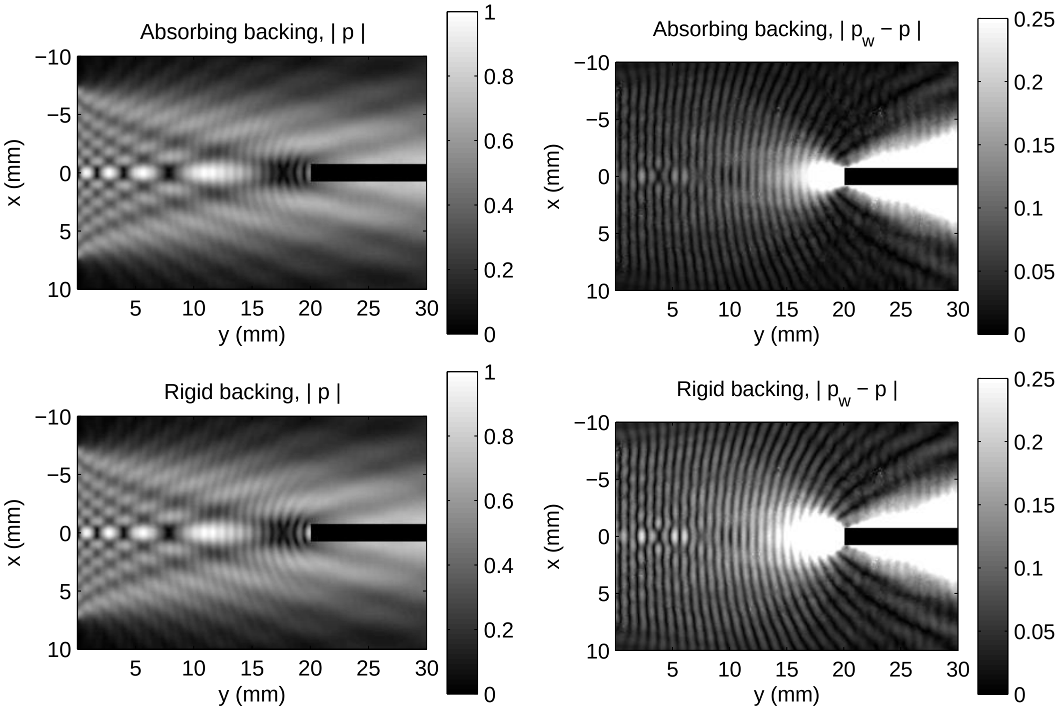

Fig. 10. The difference between absorbing (top row) and rigid backing (bottom row) materials. Figures are computed for the hydrophone 4 with $D_N = 1.47$ mm. with distance $d = 20$ mm and frequency $f = 1.0$ MHz

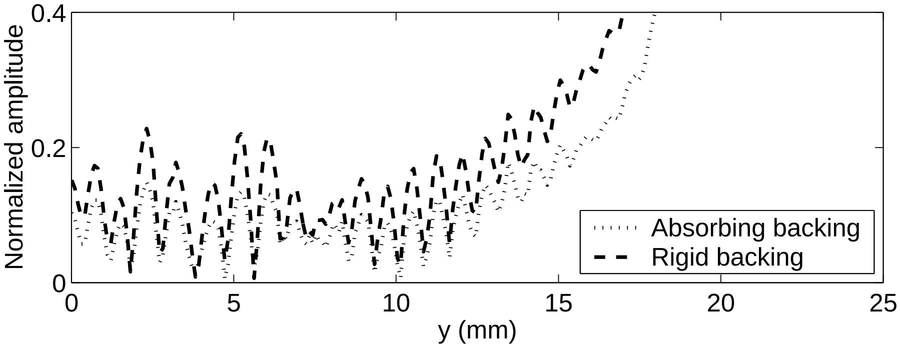

Fig. 11. Difference fields $|p_w - p|$ on the acoustic axis for absorbing and rigid backing materials ($f = 1.0$ MHz, $D_N = 1.47$ mm and $d = 20$ mm).

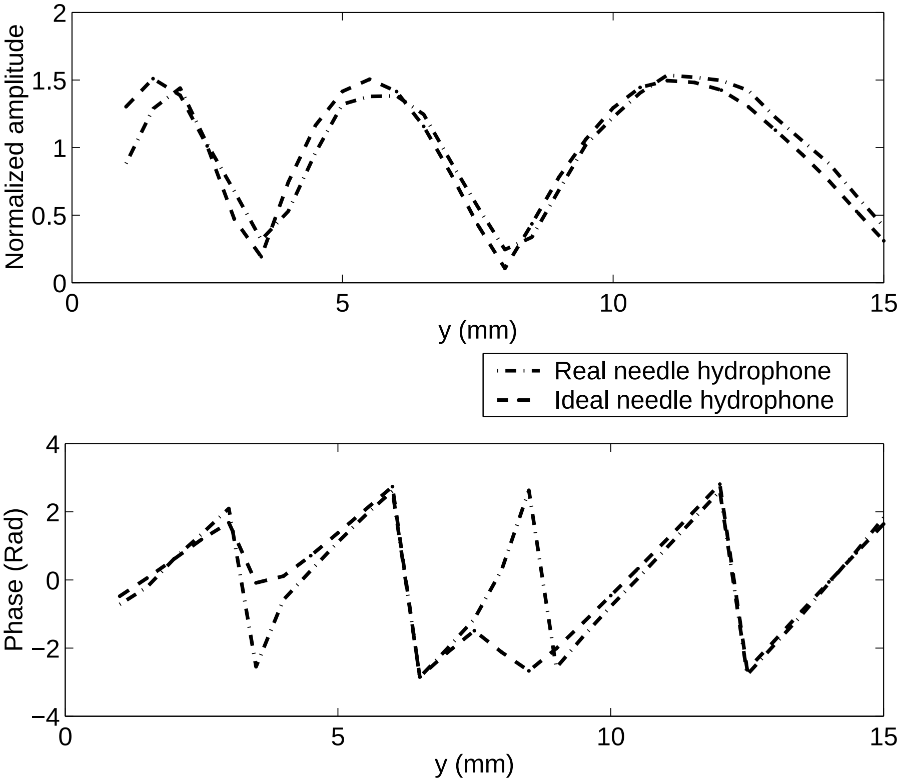

Fig. 12. Comparison of the ideal and real simulated needle hydrophone measurements on the acoustic axis of the circular source with $f = 0.5$ MHz. The diameter of the needle hydrophone is $D_N = 1.47$ mm.

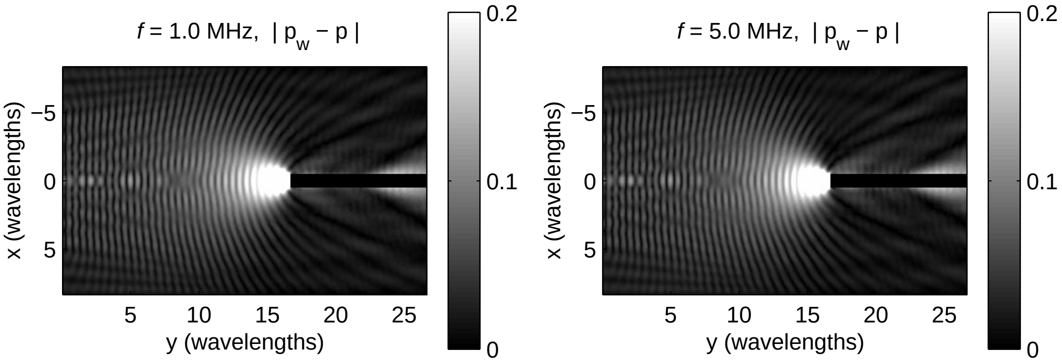

Fig. 13. The difference fields for frequencies $f = 1.0$ MHz (left) and $f = 5.0$ MHz (right). The 1.0 MHz field is computed with hydrophone 5 ($D_N = 1.5$ mm, $D_F = 0.2$ mm) at the distance $d = 25$ mm. In the case of the 5.0 MHz field, hydrophone 1 ($D_N = 0.3$ mm, $D_F = 0.04$ mm) located at the distance $d = 5$ mm.

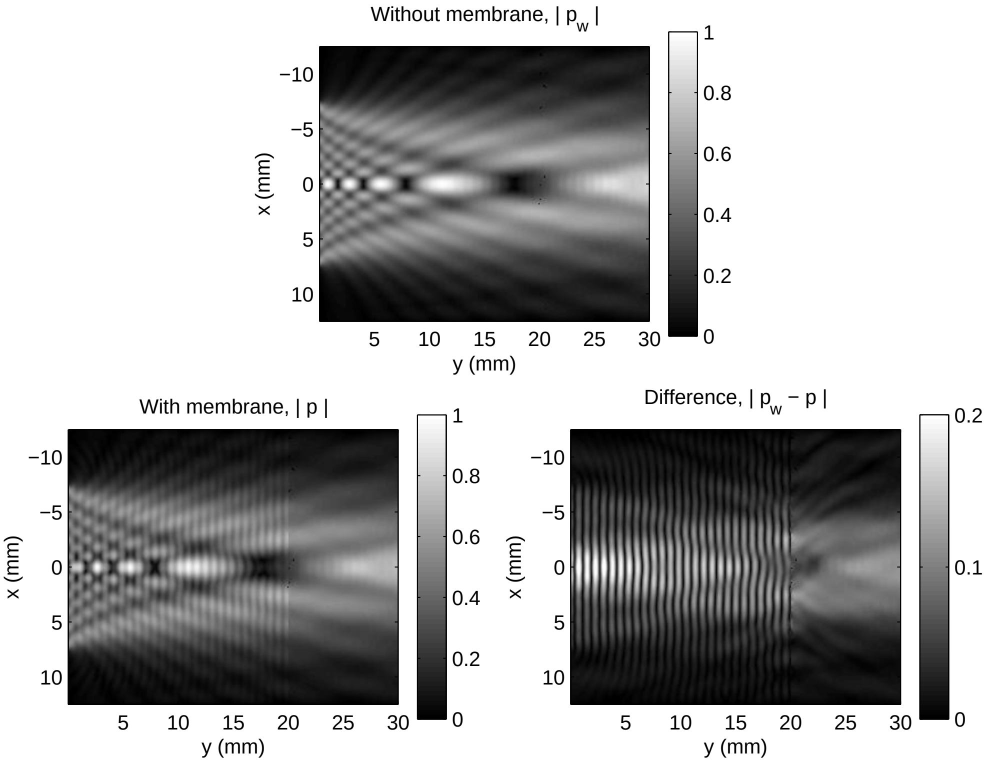

Fig. 14. The effect of the membrane hydrophone to the pressure amplitude distribution. The distance from source to membrane is $d = 20$ mm and frequency is $f = 1.0$ MHz.

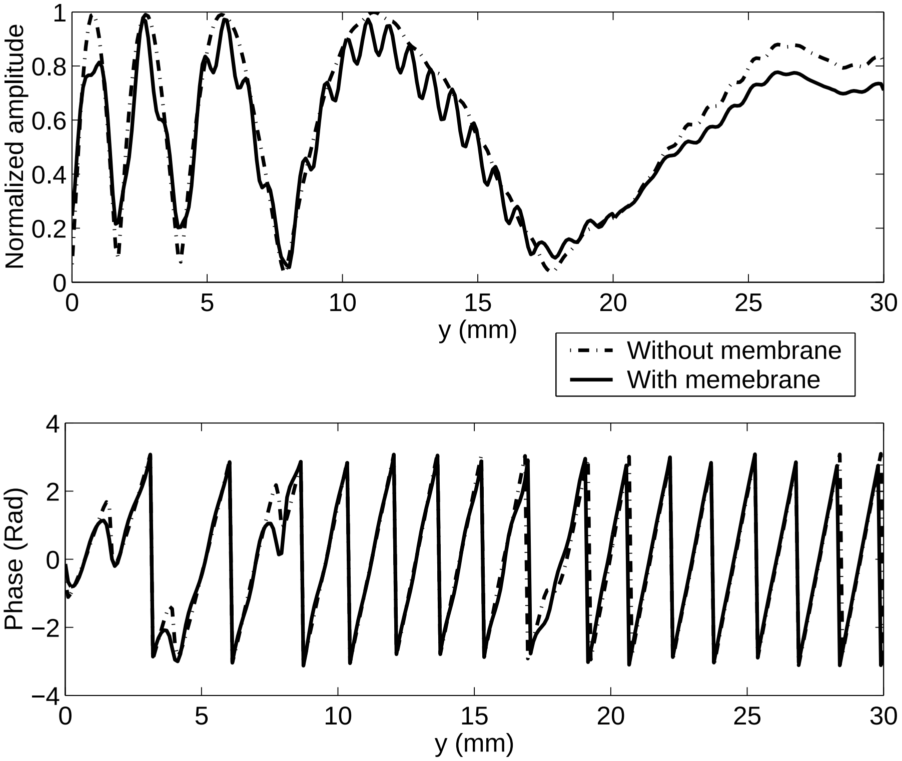

Fig. 15. Comparison of the fields with and without membrane for the frequency $f = 1.0$ MHz. The membrane is at plane $y = 20$ mm.

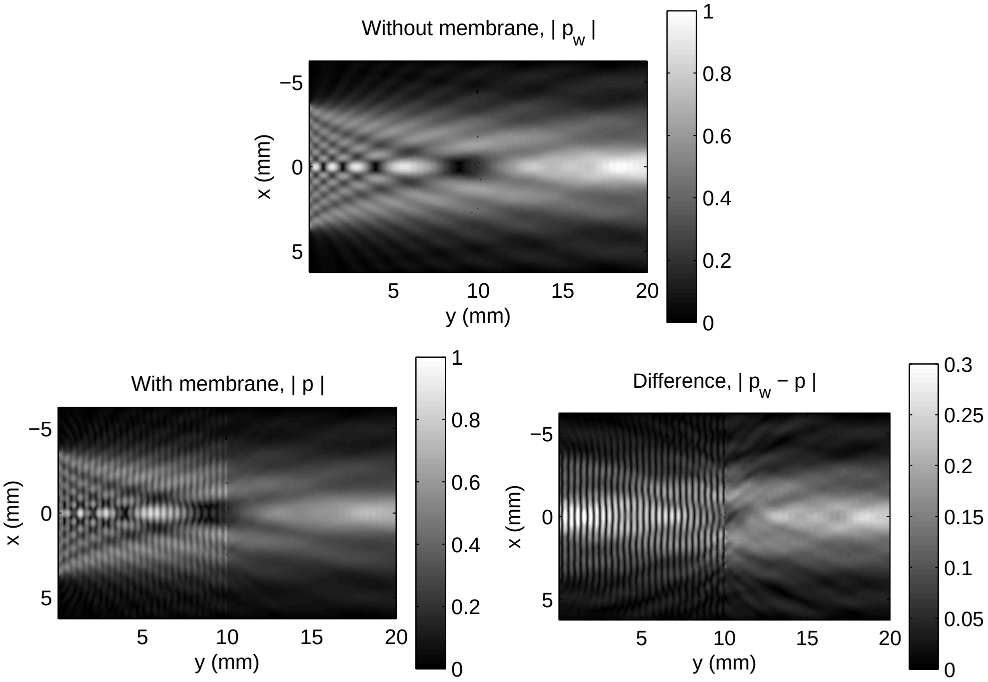

Fig. 16. The effect of the membrane hydrophone to the pressure amplitude distribution. The distance from source to membrane is $d = 10$ mm and frequency is $f = 2.0$ MHz.

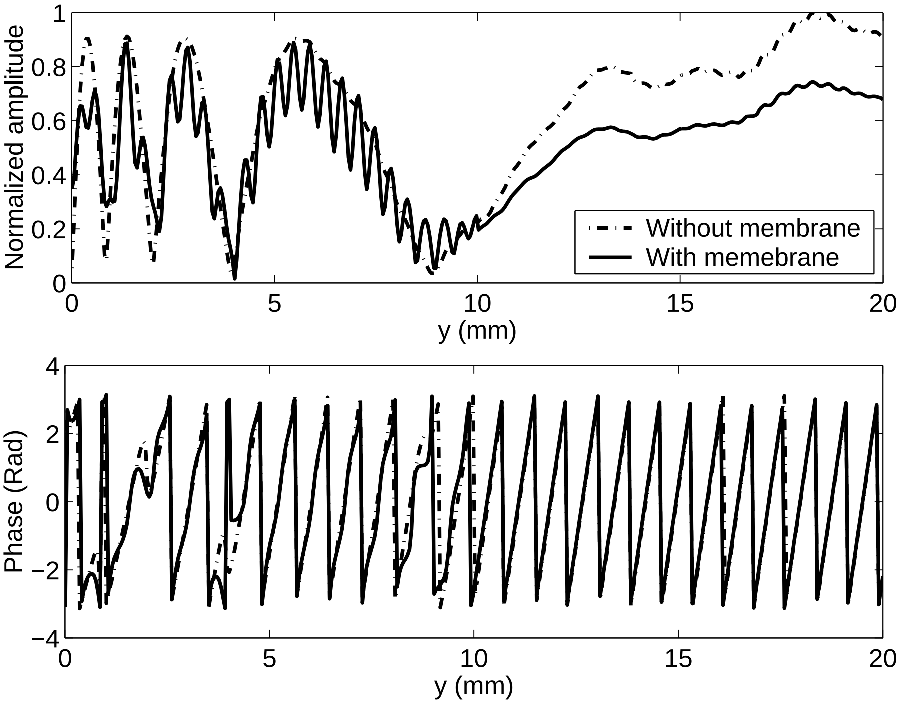

Fig. 17. Comparison of the fields with and without membrane for the frequency $f = 2.0$ MHz. The membrane is at plane $y = 10$ mm.

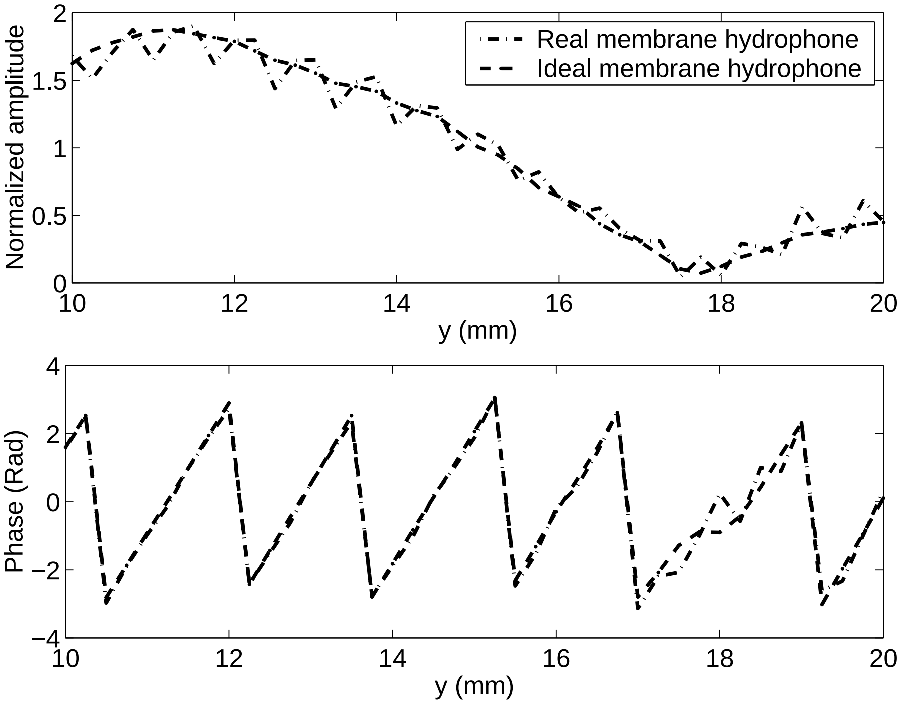

Fig. 18. Comparison of the measurements with an ideal hydrophone and real membrane hydrophone on the acoustic axis of the circular source. The frequency is $f = 1.0$ MHz.

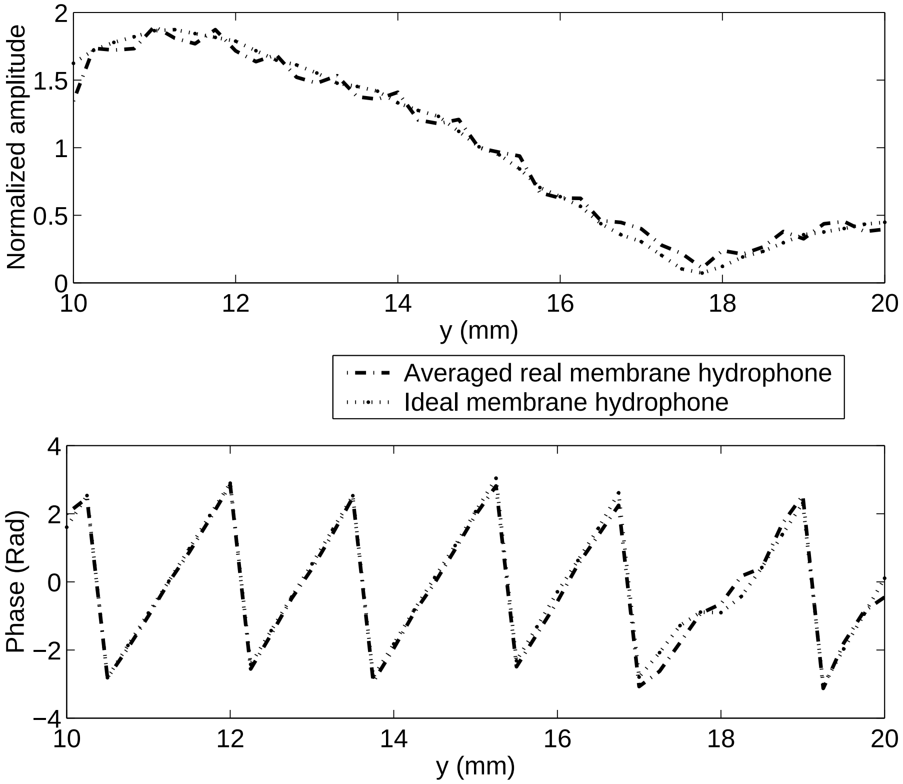

Fig. 19. By averaging the field at a given point with two adjacent points the anomalies can be diminished.

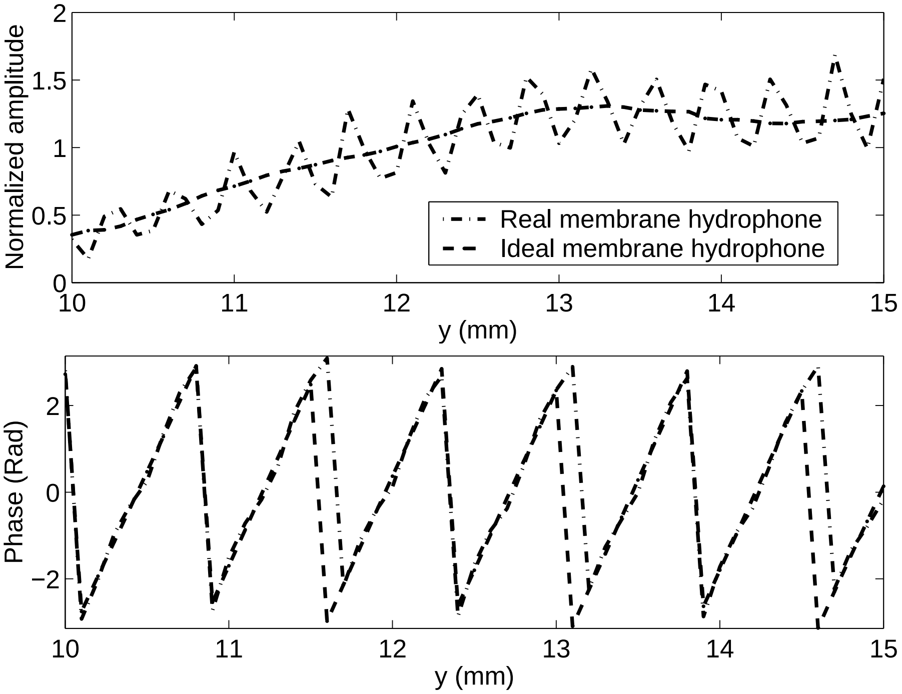

Fig. 20. Comparison of the measurements with an ideal hydrophone and the real membrane hydrophone on the acoustic axis of the circular source for $f = 2.0$ MHz.

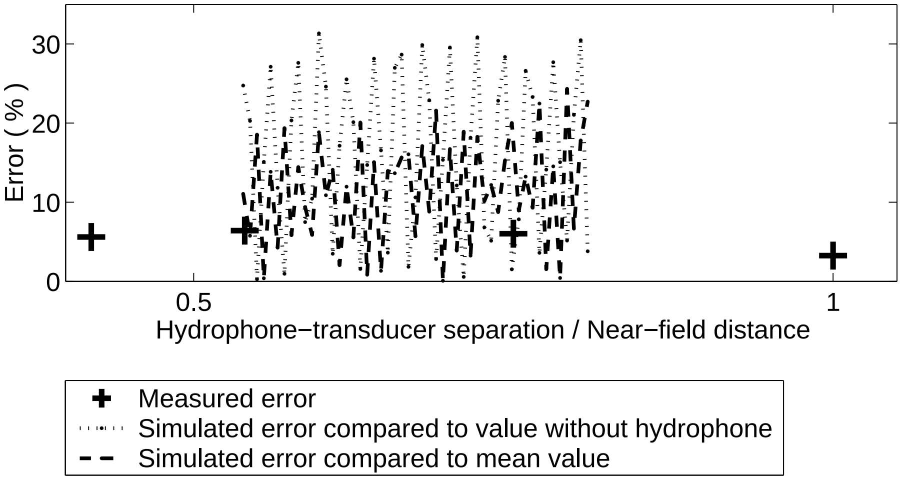

Fig. 21. The relative error in the pressure amplitude at a fixed distance (18 mm) from the 2.0 MHz transducer as a function of the transducer - membrane hydrophone separation. The membrane hydrophone scanned distances 10-15 mm with 0.1 mm spacing. The measured errors are from [8].

LIST OF TABLES

TABLE I

GEOMETRIC PARAMETERS OF THE COMPUTATION DOMAIN FOR NEEDLE HYDROPHONE SIMULATIONS.

f (MHz)	R (mm)	L (mm)	R_S (mm)
0.50	25.00	65.00	15.00
1.00	12.50	40.00	7.50
1.50	8.33	30.00	5.00
2.00	6.25	24.00	3.75
5.00	2.50	8.00	1.50

TABLE II

NEEDLE HYDROPHONES USED IN SIMULATIONS.

Hydrophone	D_N (mm)	D_F (mm)
1	0.30	0.040
2	0.30	0.075
3	0.46	0.20
4	1.47	1.00
5	1.50	0.20

TABLE III

BOUNDARY PARAMETERS IN THE UWVF SCHEME

Boundary condition, Eq.	τ	σ	g
Source, (3)	1	$\mathrm{Re}(\kappa/\rho)$	$-2i\omega v_n$
Rigid, (4)	1	$\mathrm{Re}(\kappa/\rho)$	0
Absorbing, (5)	0	$\mathrm{Re}(\kappa/\rho)$	0